nature biotechnology

A 3D bioprinting system to produce human-scale tissue constructs with structural integrity

Hyun-Wook Kang, Sang Jin Lee, In Kap Ko, Carlos Kengla, James J Yoo & Anthony Atala

A challenge for tissue engineering is producing three-dimensional (3D), vascularized cellular constructs of clinically relevant size, shape and structural integrity. We present an integrated tissue–organ printer (ITOP) that can fabricate stable, human-scale tissue constructs of any shape. Mechanical stability is achieved by printing cell-laden hydrogels together with biodegradable polymers in integrated patterns and anchored on sacrificial hydrogels. The correct shape of the tissue construct is achieved by representing clinical imaging data as a computer model of the anatomical defect and translating the model into a program that controls the motions of the printer nozzles, which dispense cells to discrete locations. The incorporation of microchannels into the tissue constructs facilitates diffusion of nutrients to printed cells, thereby overcoming the diffusion limit of 100–200 μm for cell survival in engineered tissues. We demonstrate capabilities of the ITOP by fabricating mandible and calvarial bone, cartilage and skeletal muscle. Future development of the ITOP is being directed to the production of tissues for human applications and to the building of more complex tissues and solid organs.

© 2016 Nature America, Inc. All rights reserved.

The demand for engineered tissues has risen rapidly owing to the limited availability of donor tissues and organs for transplantation. Despite some initial successes in engineering relatively simple tissues, many challenges remain in developing tissues and organs suitable for clinical translation[1,2]. Three-dimensional (3D) printing technology shows promise for creating complex composite tissue constructs[3–8] through precise placement of cell-laden hydrogels in a layer-by-layer fashion[7,9–17]. The most commonly used bioprinting systems are based on jetting, extrusion and laser-induced forward transfer (LIFT)[6,18,19]. The jetting method produces picoliter scale drops with a printing resolution of 20~100 μm. However, because the hydrogel concentration is low[20–23], the thickness of printed constructs may be limited because of inadequate structural support[24]. Extrusion methods, which use a syringe and piston system to dispense material through microscale nozzles, can produce more stable 3D cell-laden structures using high concentrations of hydrogels such as alginate, fibrin and Pluronic F-127 (refs. 18,25–27). However, it is difficult to construct large free-form tissue structures owing to inadequate structural integrity, mechanical stability and printability[28–30]. The LIFT method can precisely print cells in relatively small constructs[31] but requires rapid gelation of hydrogels to achieve high resolution of the printed patterns, resulting in low flow rates.

Here we describe a system that deposits cell-laden hydrogels together with synthetic biodegradable polymers that impart mechanical strength, thereby overcoming previous limitations on the size, shape, structural integrity and vascularization of bioprinted tissue constructs. This was accomplished by designing multidispensing modules for delivering various cell types and polymers in a single construct; by developing an optimized carrier material for delivering cells to discrete locations in the 3D structure in a liquid form; by designing sophisticated nozzle systems with a resolution down to 2 μm for biomaterials and down to 50 μm for cells; by cross-linking cell-laden hydrogels after passage though the nozzle system; by simultaneously printing an outer sacrificial acellular hydrogel mold that is dissolved after the tissue construct acquires enough rigidity to retain its shape; and by creating a lattice of microchannels permissive to nutrient and oxygen diffusion into the printed tissue constructs. These properties, all designed to work in a coordinated manner, make up the ITOP. We demonstrate the printer by fabricating human-scale mandible bone, ear-shaped cartilage and organized skeletal muscle. Evaluation of the characteristics and function of these tissues *in vitro* and *in vivo* showed tissue maturation and organization that may be sufficient for translation to patients.

RESULTS

Design of the ITOP system

Multiple cartridges (**Fig. 1a** and **Supplementary Fig. 1**) are used to deliver and pattern multiple cell-laden composite hydrogels, supporting poly(ε-caprolactone) (PCL) polymer and a sacrificial Pluronic F-127 hydrogel (**Fig. 1b**). The end of each cartridge is connected to a microscale nozzle, and the top is connected to an air pressure controller for precisely controlling the dispensing volume. A heating unit ensures that the PCL remains easily dispensable. A three-axis motorized stage system enables 3D patterning of multiple cells and biomaterials. The system resides in a humidified and temperature-controlled (18 °C) enclosure.

The correct shape of a tissue construct is obtained from a human body by processing computed tomography (CT) or magnetic resonance imaging (MRI) data in computer-aided design (CAD) software (**Fig. 1c**). A custom nozzle motion program is generated by incorporating

Wake Forest Institute for Regenerative Medicine, Wake Forest School of Medicine, Medical Center Boulevard, Winston-Salem, North Carolina, USA. Correspondence should be addressed to A.A. (aatala@wakehealth.edu).

Received 27 July 2015; accepted 19 October 2015; published online 15 February 2016; doi:10.1038/nbt.3413

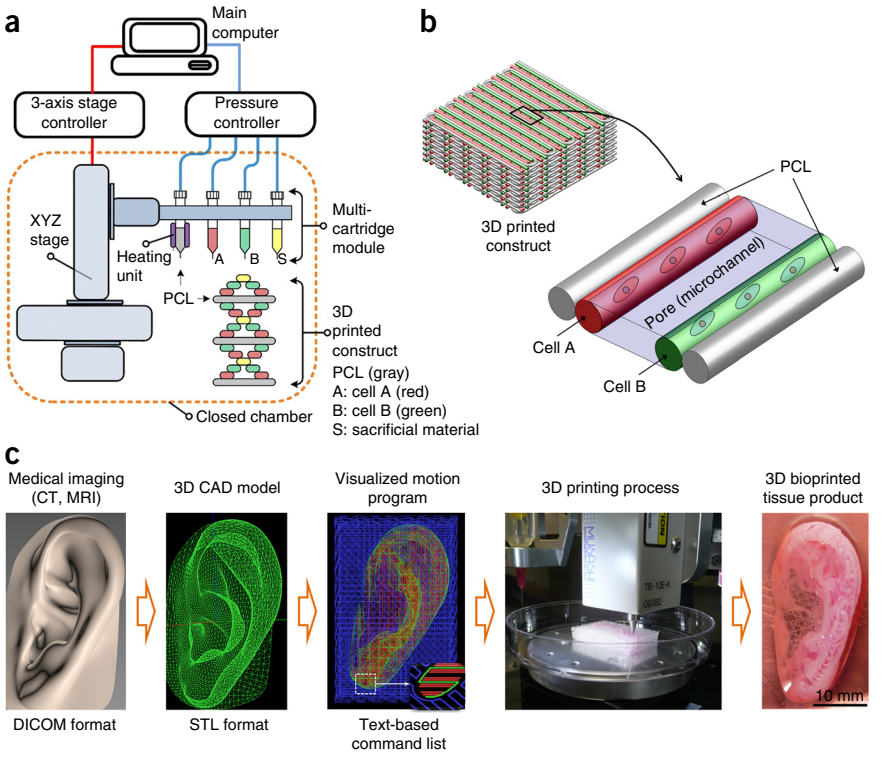

Figure 1 ITOP system. (**a**) The ITOP system consists of three major units: (i) 3-axis stage/controller, (ii) dispensing module including multi-cartridge and pneumatic pressure controller and (iii) a closed acrylic chamber with temperature controller and humidifier. (**b**) Illustration of basic patterning of 3D architecture including multiple cell-laden hydrogels and supporting PCL polymer. (**c**) CAD/CAM process for automated printing of 3D shape imitating target tissue or organ. A 3D CAD model developed from medical image data generates a visualized motion program, which includes instructions for XYZ stage movements and actuating pneumatic pressure to achieve 3D printing.

the printing pattern in combination with fabrication conditions (for example, scan speed, temperature, material information and air pressure). The ITOP uses a text-based motion program consisting of a command list for XYZ stage movements and air pressure actuation (**Supplementary Source Code**). The motion program is then transferred to the main computer of the 3D printing system that effects the biofabrication process.

The composite hydrogel for cell delivery consisted of gelatin, fibrinogen, hyaluronic acid (HA) and glycerol mixed into DMEM (high glucose). We tested various concentrations of each component to achieve proper printing resolution and dispensing uniformity, mechanical properties (before and after cross-linking with thrombin) and cell viability (**Supplementary Fig. 2**). The optimized concentrations of hydrogel ingredients and the numbers of cells needed for fabrication of individual tissue constructs are listed in **Table 1**.

Patterning synthetic polymers confers mechanical strength

Our first series of studies tested the ability of the ITOP to generate uniform two-dimensional (2D) and 3D cell patterns of multiple cell types. Using 3T3 fibroblasts labeled with two fluorescent dyes, DiI (red) and DiO (green), we demonstrated delivery of the two populations in a unique 2D pattern (**Fig. 2a**,**b**). To create 3D constructs, we combined the fluorescently labeled 3T3 fibroblasts in composite hydrogels with supporting PCL and printed them in two patterns—type I (**Fig. 2c**) and type II (**Fig. 2f**). These patterns differ in the placement of PCL and thus in the mechanical strength of the printed construct. The type I pattern creates multiple PCL frames in each layer throughout the construct, and places cells and gel materials in between the frames. The type II pattern consists of cell-laden hydrogel and porous structures, surrounded by a PCL framework on the outer layers and corners of each layer, thus protecting the contents from external load. Type I constructs (**Fig. 2d**,**e**) maintained a more stable structure than type II constructs (**Fig. 2g**,**h**), owing to the abundance of uniformly distributed PCL frames. Therefore, we used the type I pattern to fabricate mandible bone and ear-shaped cartilage structures and the type II pattern to print organized skeletal muscle constructs.

Next, we produced 3D structures by placing either type I or type II patterns of cell-laden hydrogel and PCL (~130 μm for type I and ~250 μm wide for type II). The microchannels (type I: 500 × 300 μm^2; type II: 650 × 450 μm^2), formed by the PCL patterns, were designed to maximize diffusion of nutrients and oxygen. In addition, we used Pluronic F-127 hydrogel as a sacrificial outer layer to support the 3D architecture of the dispensed cell-laden structures before crosslinking. After cross-linking of fibrinogen using thrombin, the uncross-linked components (gelatin, HA, glycerol and Pluronic F-127) were washed out.

To determine cell viability during printing, we examined survival of 3T3 fibroblasts at 60 min (day 0), 3 d and 6 d after printing. Live/dead cell assays showed ≥95% cell viability on day 0, which was maintained through days 3 and 6 (**Fig. 2i**). Cell proliferation, assessed using the AlamarBlue assay system, increased over a 15-d period, similar to the proliferation of control cells encapsulated in a fibrin construct (**Fig. 2j**). These data indicate that the optimized composite hydrogel system maintained cell viability during the printing process and provided a favorable microenvironment for cell proliferation.

Mandible bone reconstruction

To demonstrate construction of a human-sized bone structure, we fabricated a mandible fragment in a size and shape similar to what would be needed for facial reconstruction after traumatic injury (**Fig. 3**). The cell type used was human amniotic fluid–derived stem cells

Table 1 Preparation of the cell-laden composite hydrogels for 3D bioprinted tissue constructs

	Composite hydrogel						
	Gelatin	Fibrinogen	HA	Glycerol	Cell type & density	Cell viability	Remark
Bone (type I)	35 mg/ml	20 mg/ml	3 mg/ml	10% v/v	Human AFSCs, 5 × 10^6 cells/ml	91 ± 2% (day 1)	**Figs. 3** and **4**
Cartilage (Type I)	45 mg/ml	30 mg/ml	3 mg/ml	10% v/v	Rabbit ear chondrocytes, 40 × 10^6 cells/ml	91 ± 8% (day 1)	**Fig. 5**
Skeletal muscle (type II)	35 mg/ml	20 mg/ml	3 mg/ml	10% v/v	Mouse C2C12 myoblasts, 3 × 10^6 cells/ml	97 ± 6% (day 1)	**Fig. 6**

© 2016 Nature America, Inc. All rights reserved.

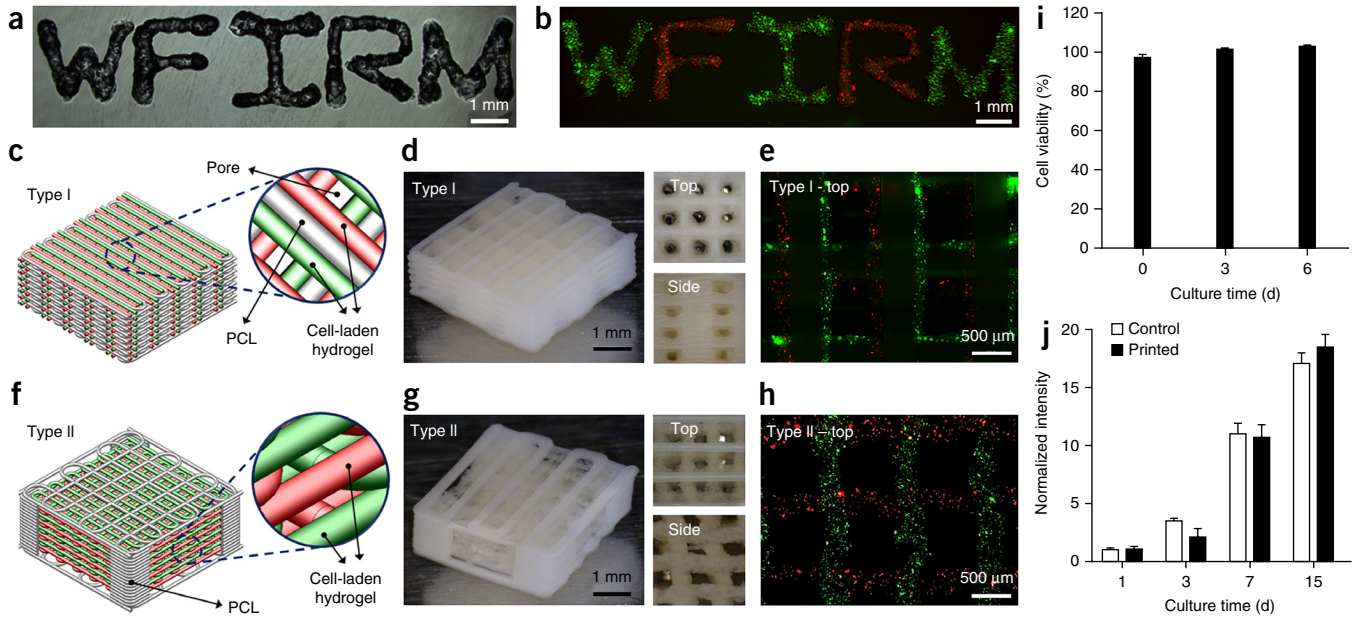

Figure 2 2D/3D patterning using the ITOP system. (**a**,**b**) 2D patterning of 'WFIRM' characters written by cell-laden hydrogels through the integrated organ printing. Microscopic (**a**) and fluorescent images (**b**) of 'WFIRM' characters, which were produced using cells labeled with DiI and DiO. (**c**–**h**) Two basic types of 3D patterning: type I pattern (**c**–**e**) and type II pattern (**f**–**h**). Two types of 3D patterning, including cell-A (red), cell-B (blue) and PCL (green), were fabricated by the integrated organ printing (**c**,**f**); photographs (**d**,**g**) and fluorescent image (**e**,**h**) of the 3D printed patterns. (**i**) Cell viability was over 95% on day 0 and then maintained on days 3 and 6 ($n = 3$). (**j**) Cell proliferation results showed that the number of cells continuously increased over a 15-d period, and no significant differences between the control and the printed constructs were observed ($n = 5$). Error bars, mean ± s.d.

(hAFSCs), which can give rise to osteogenic lineages in appropriate media[32,33]. Mandible bone defects have an arbitrary shape. We used data from a CT scan of a human mandible defect in combination with Mimics software (Materialise, Leuven, Belgium) to produce a CAD model of the defect shape, with dimensions of 3.6 cm × 3.0 cm × 1.6 cm (**Fig. 3a**). A text-based command motion program, generated from the CAD model with custom CAM software, determined the required dispensing paths of cell-laden hydrogel, a mixture of PCL and tricalcium phosphate (TCP), and Pluronic F127 (**Fig. 3b**). PCL/TCP and hAFSCs mixed with the composite hydrogel (**Table 1**) were printed in a type I pattern with a Pluronic F127 temporary support (**Fig. 3c**). At 1 d of culture, cell viability in the printed bone structures was 91 ± 2% ($n = 3$, **Table 1**), confirming that the printing process did not adversely affect cell viability. After induction of osteogenic differentiation using an established protocol[32,33] for 28 d ($n = 5$, **Fig. 3d**), we stained the structures with Alizarin Red S; staining at the surface of the 3D bone structures indicated calcium deposition in the hAFSC-laden hydrogel (**Fig. 3e**). 3D constructs before differentiation showed no Alizarin Red S staining (data not shown).

Calvarial bone reconstruction

To study maturation of the bioprinted bone *in vivo*, we fabricated rat calvarial bone constructs in a circular shape (8 mm diameter × 1.2 mm thickness) with hAFSCs (**Fig. 4a**,**b** and **Supplementary Fig. 3**), cultured them in osteogenic media for 10 d, implanted them in a calvarial bone defect region of Sprague Dawley rats ($n = 4$) and analyzed them 5 months after implantation (**Fig. 4c**).

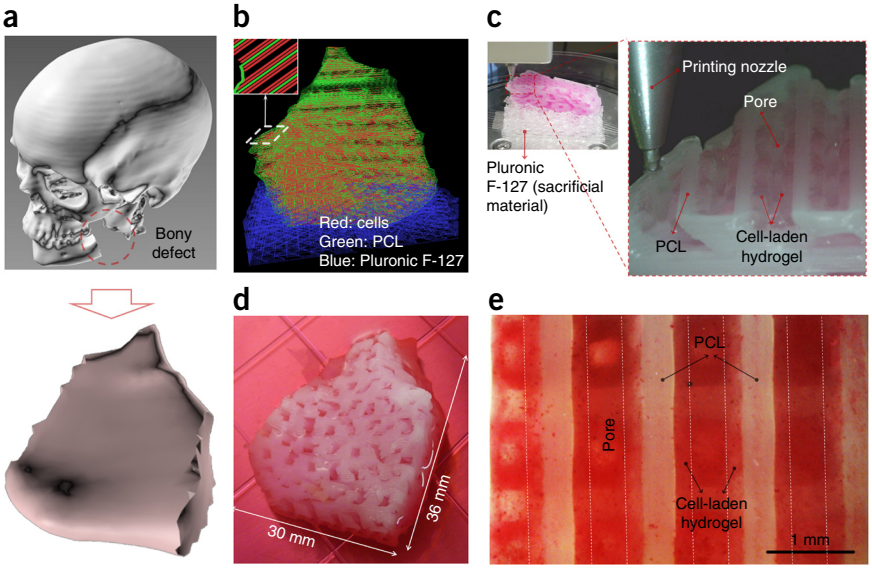

Figure 3 Mandible bone reconstruction. (**a**) 3D CAD model recognized a mandible bony defect from human CT image data. (**b**) Visualized motion program was generated to construct a 3D architecture of the mandible bone defect using CAM software developed by our laboratory. Lines of green, blue and red colors indicate the dispensing paths of PCL, Pluronic F-127 and cell-laden hydrogel, respectively. (**c**) 3D printing process using the integrated organ printing system. The image shows patterning of a layer of the construct. (**d**) Photograph of the 3D printed mandible bone defect construct, which was cultured in osteogenic medium for 28 d. (**e**) Osteogenic differentiation of hAFSCs in the printed construct was confirmed by Alizarin Red S staining, indicating calcium deposition.

© 2016 Nature America, Inc. All rights reserved.

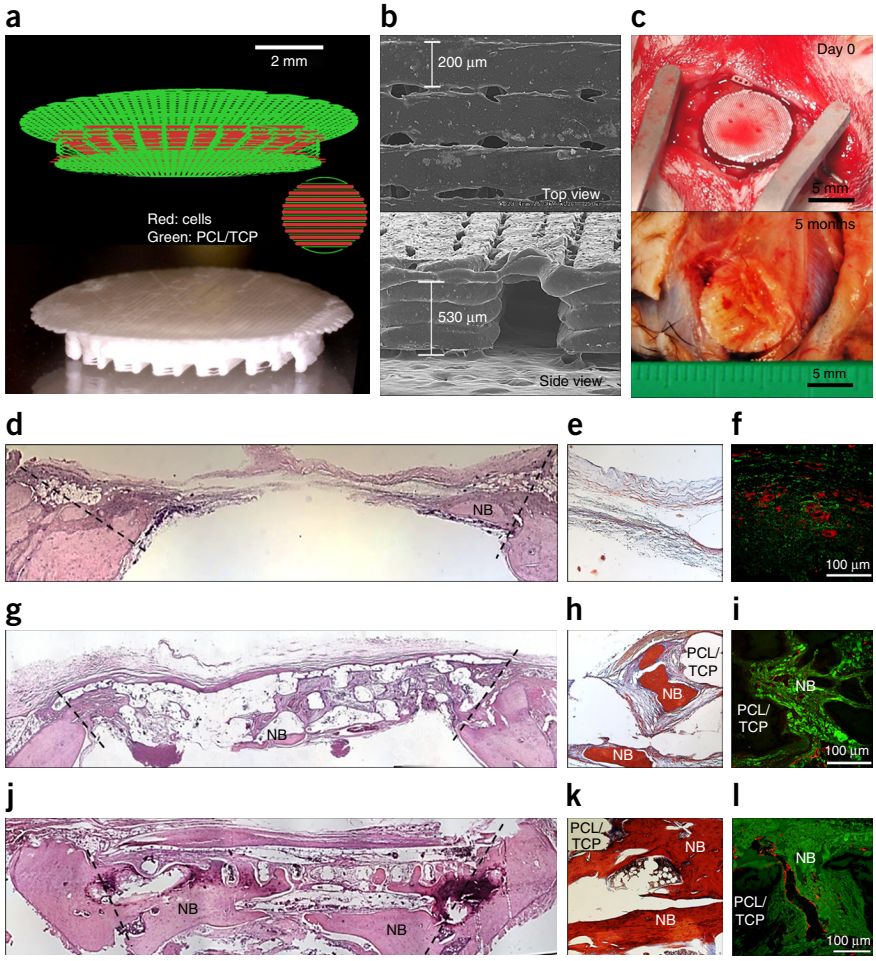

Figure 4 Calvarial bone reconstruction. (**a**) Visualized motion program (top) used to print a 3D architecture of calvarial bone construct. Green and red color lines indicate the dispensing paths of the PCL/TCP mixture and cell-laden hydrogel, respectively. Photograph of the printed calvarial bone construct (bottom). (**b**) Scanning electron microscope images of the printed bone constructs. (**c**) Photographs of the printed bone constructs at day 0 (top) and 5 months (bottom) after implantation. (**d**–**l**) Histological and immunohistological images of nontreated (**d**–**f**), scaffold only without cells (**g**–**i**) and hAFSCs-printed construct at 5 months after implantation (**j**–**l**). H&E staining (**d**,**g**,**j**), modified tetrachrome staining (**e**,**h**,**k**) and vWF immunostaining (**f**,**i**,**l**). Tetrachrome staining: red, mature bone; blue, osteoid and lining of lacunae. vWF immunofluorescent image: red, blood vessel. NB: new bone; PCL/TCP: remaining scaffold.

The bioprinted constructs showed newly formed vascularized bone tissue throughout the implants, including the central portion, with no necrosis (**Fig. 4j**), whereas the untreated defect and scaffold-only treated control groups showed fibrotic tissue ingrowth (**Fig. 4d**) and minimal bone tissue formation restricted to the periphery of the implant (**Fig. 4g**), respectively. The modified Tetrachrome staining confirmed mature bone (red) and osteoid (blue) formation (**Fig. 4e**,**h**,**k**). Von Willebrand factor (vWF) immunostaining showed large blood vessel formation within newly formed bone tissue throughout the bioprinted bone constructs, including the central portion (**Fig. 4l**), whereas the nontreated (**Fig. 4f**) and scaffold-only (**Fig. 4i**) groups had only limited vascularization restricted to the periphery of the implant.

Ear cartilage reconstruction

Next, we tested the ability of the ITOP to fabricate tissue constructs of complex shape by making human-sized external ears, as the framework of an auricle consists of a single piece of cartilage with a complicated geometry of ridges. A CT image of an ear (**Fig. 5a**) was used to develop a motion program (**Fig. 5b**) to print a chondrocyte-laden hydrogel, PCL and Pluronic F-127. Using rabbit ear chondrocytes (passages 3 and 4) mixed with the composite hydrogel (**Table 1**), we fabricated human ear–shaped cartilage constructs with dimensions of 3.2 cm × 1.6 cm × 0.9 cm (**Fig. 5c**–**e**) in the type I pattern. Cell viability was 91 ± 8% at 1 d after printing (n = 3, **Table 1**). After 5 weeks in the culture medium, the constructs were stained with Safranin-O and showed production of a new cartilaginous matrix (**Fig. 5f**). The constructs with microchannels showed enhanced tissue formation as evidenced by the production of new viable cartilaginous matrix throughout the entire ear constructs. In contrast, the constructs without microchannels showed only limited tissue formation restricted to the peripheral region, likely owing to the diffusion limits of nutrients and oxygen. The cells in the newly formed tissues demonstrated similar morphological characteristics to those in native ear cartilage, with cells located within typical chondrocyte lacunae, surrounded by a cartilaginous matrix (**Fig. 5g**). Native human ear tissue served as a positive control.

To determine whether the printed ear constructs would mature *in vivo*, we implanted them in the dorsal subcutaneous space of athymic mice and retrieved them 1 and 2 months after implantation (n = 4). The shape was well maintained, with substantial cartilage formation upon gross examination (**Fig. 5h**). Histological analysis showed the formation of cartilage tissue (**Fig. 5i**). The glycosaminoglycan (GAG) content (2.7 ± 0.2 µg/mg at 1 month and 4.2 ± 0.3 µg/mg at 2 months) increased over time, reaching 20% of that of native ear GAG content (**Fig. 5j**). Vascularization of the printed constructs in the outer region was suggested by endothelial cell marker expression at 1 and 2 months after implantation (**Supplementary Fig. 4**). The inner regions were avascular (**Supplementary Fig. 4**), as in native cartilage, but the cartilage cells were viable, suggesting adequate nutrient diffusion during development. Biomechanical analyses (n = 4, **Fig. 5k**) showed that maturation *in vivo* strengthened the tissue constructs, resulting in a higher normalized load during bending compared with pre-implant constructs. In addition, resilience, measured by the ΔLoad%, was tested by repeated bending and relaxation cycles. Resilience between the repeated bending cycles was much higher in the constructs implanted for 1 month (**Fig. 5m** and **Supplementary Table 1**) than in the constructs before implantation (**Fig. 5l**) . These results demonstrate the generation of ear-shaped cartilage with resilience properties similar to those of native cartilage (rabbit ear) (**Supplementary Table 1**).

Skeletal muscle reconstruction

Finally, we applied the ITOP to fabricate an organized soft tissue—a 3D muscle construct 15 mm × 5 mm × 1 mm in dimension containing

© 2016 Nature America, Inc. All rights reserved.

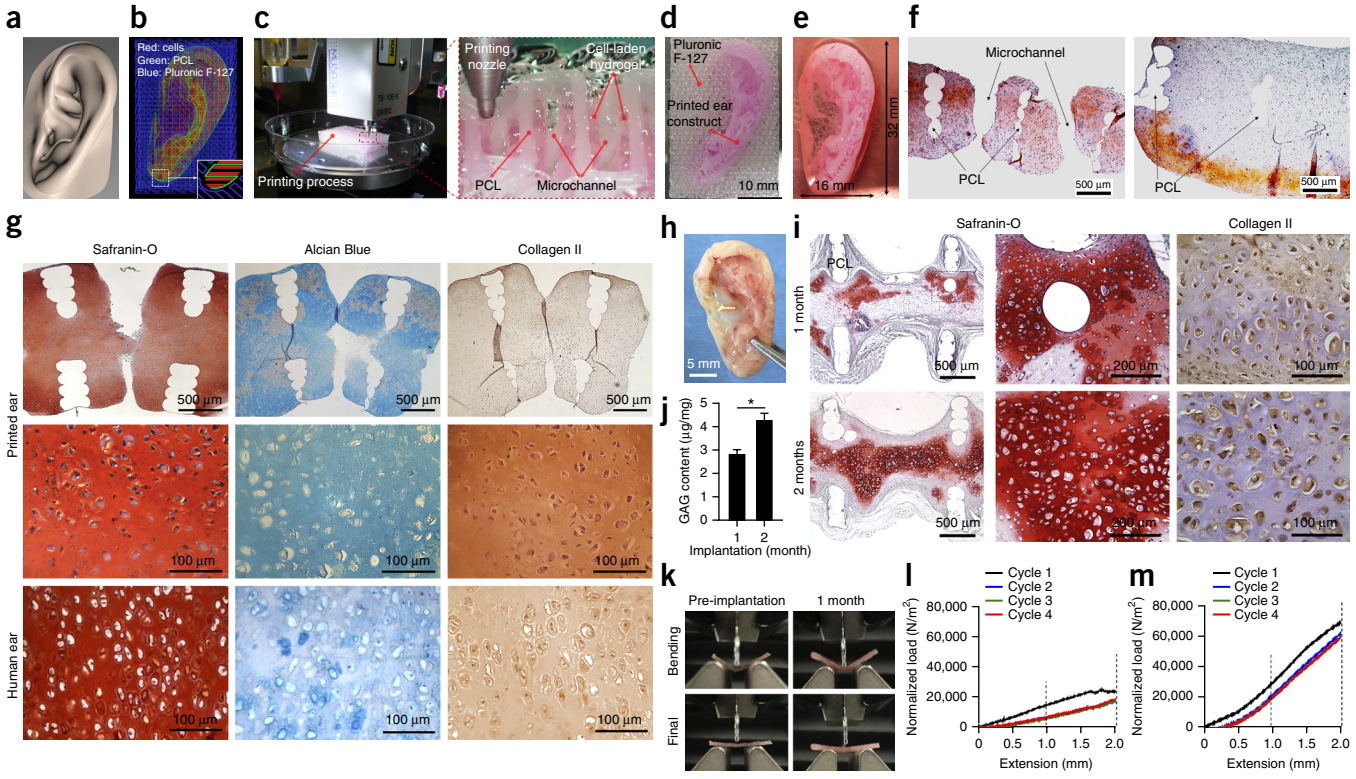

Figure 5 Ear cartilage reconstruction. (**a**–**f**) *In vitro* bioprinted ear construct. (**a**) 3D CAD of a human ear. (**b**) Visualized motion program used to print 3D architecture of human ear. The motion program was generated by using 3D CAD model. Lines of green, blue and red indicate dispensing paths of PCL, Pluronic F-127 and cell-laden hydrogel, respectively. (**c**) 3D printing process using the integrated organ printing system (**Supplementary Movie 1**). The image shows patterning of a layer of the construct. (**d**,**e**) Photographs of the 3D printed ear cartilage construct with sacrificial Pluronic F-127 (**d**) and after removing sacrificial material by dissolving with cold medium (**e**). (**f**) Safranin-O staining of the 3D printed cartilage constructs with microchannels (porous; left) and without microchannels (nonporous; right) after culture in chondrogenic medium for 5 weeks *in vitro*. The constructs with microchannels showed the production of new cartilaginous matrix throughout the entire constructs, whereas the constructs without microchannels showed limited tissue formation due to limited diffusion of nutrients and oxygen. The staining indicates the production of GAGs. (**g**) Safranin-O staining, Alcian Blue staining and immunohistochemistry for type II collagen of the 3D printed ear cartilage constructs after culture in chondrogenic medium for 5 weeks *in vitro*. Histological images of the samples showed the production of a new cartilaginous matrix within the 3D printed constructs. The chondrocytes in the newly formed tissue demonstrated similar morphological characteristics to those in native cartilage, with cells located within typical chondrocyte lacunae, surrounded by cartilaginous matrix. The newly formed matrix generated in the constructs stained intensely with Safranin-O and Alcian Blue, showing the presence of sulfated proteoglycans. Immunohistochemical staining indicated the presence of type II collagen in the constructs. Human ear was used a positive control. (**h**–**m**) *In vivo* bioprinted ear construct. (**h**,**i**) Gross appearance at 1 month after implantation (**h**), Safranin-O staining and collagen type II immunostaining (**i**) of the retrieved ear construct at 1 month and 2 months after implantation. (**j**) GAG contents of the bioprinted ear cartilage tissues after 1 and 2 months of implantation. Error bars, mean ± s.d. (**k**) Gross examination of bending testing of the bioprinted ear constructs: pre-implantation vs. 1-month implantation. (**l**,**m**) Stress-strain curve of pre-implanted construct (**l**) and1-month implanted construct under four-cycle three-point bending test (**m**).

mouse myoblasts (**Table 1**) printed in the type II pattern (**Fig. 6a**,**b**). Immediately after printing, the printed structures contained muscle fiber–like bundles (~400 μm width), supporting PCL pillars and Pluronic F-127 hydrogel as a temporary structure (**Fig. 6c** and **Supplementary Fig. 5a**). Notably, the printed cells began stretching along the longitudinal axis of the constructs at day 3 in growth media (**Fig. 6e** and **Supplementary Fig. 5b**) with high cell viability (**Fig. 6f**), and the constructs underwent compaction[34], keeping the fibers taut during cell growth and differentiation, whereas the printed cells without PCL support did not show cellular alignment (**Fig. 6d**). After 7 d in differentiation media, muscle-like structures with aligned myotubes were observed (**Fig. 6g** and **Supplementary Fig. 5c**).

To study whether these structures could mature into functional muscle *in vivo*, we implanted 7-d differentiated structures subcutaneously (ectopically) in 14- to 16-week-old nude rats ($n = 6$). The dissected distal end of the proximal stump of the common peroneal nerve (CPN) was embedded within the constructs to promote integration (**Fig. 6h**,**i**). Adequate innervation of implanted muscle is essential to achieve and maintain muscle function. Our model allowed us to evaluate nerve integration of the implanted muscle construct independent of the surrounding muscle tissue. After 2 weeks of implantation, the retrieved muscle constructs showed well-organized muscle fiber structures (**Fig. 6j**), the presence of acetylcholine receptor (AChR) clusters on the muscle fibers (MHC^+ and $\alpha\text{-}BTX^+$) (**Fig. 6k**), as well as nerve (neurofilament) contacts with $\alpha\text{-}BTX^+$ structures within the implants (**Fig. 6l**), indicating that the printed muscle constructs were robust enough to maintain their structural characteristics and induce nerve integration *in vivo*. In addition, vascularization throughout the muscle constructs was indicated by endothelial cell marker expression (**Fig. 6m**). To examine muscle function, we performed electromyography to evaluate electrical and neurological activation of the constructs 2 weeks after implantation. Compound muscle action potential, which is evoked by motor nerves and measures muscle function, was 3.6 mV, compared to 10.7 mV for the control gastrocnemius muscle, and

© 2016 Nature America, Inc. All rights reserved.

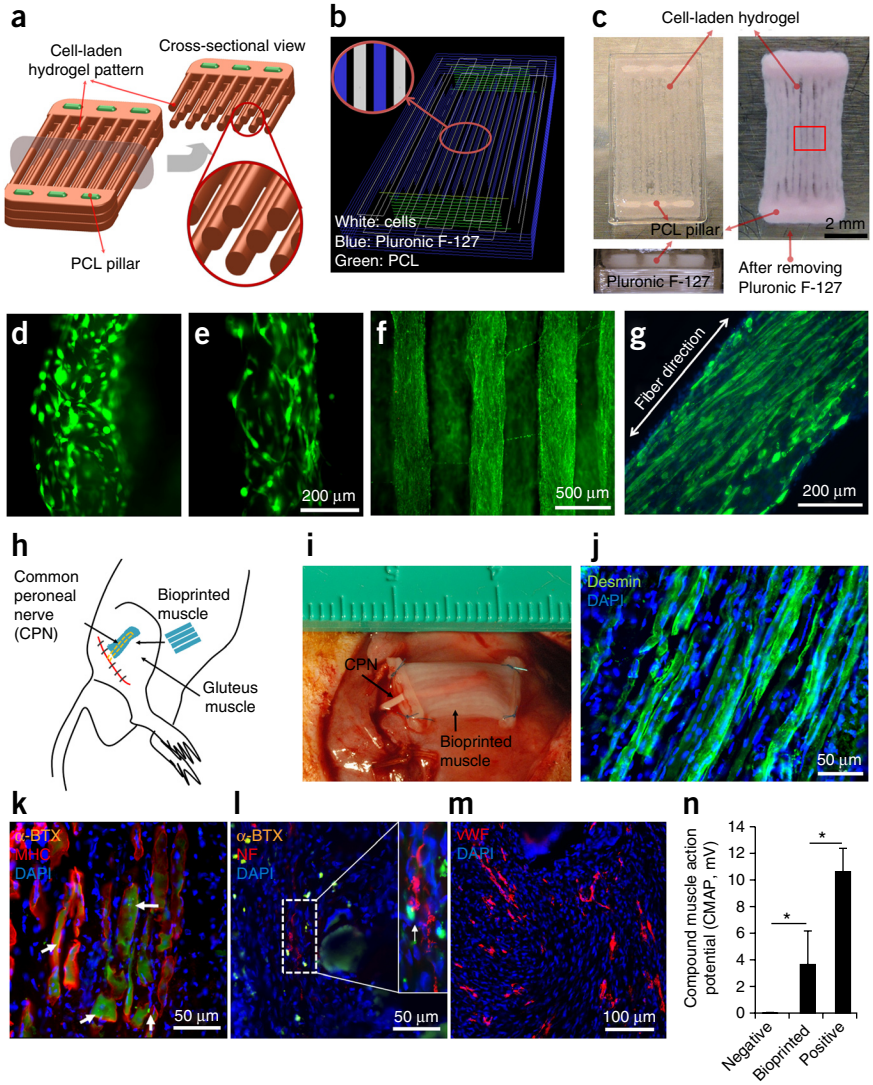

Figure 6 Skeletal muscle reconstruction. (**a**–**g**) *In vitro* bioprinted muscle. (**a**) Designed fiber bundle structure for muscle organization. PCL pillars (green) were used to maintain the structure and to induce the compaction phenomenon for cell alignment. (**b**) Visualized motion program for 3D printing muscle construct. Lines of green, white and blue indicate the dispensing paths of PCL, cell-laden hydrogel and sacrificial material, respectively. (**c**) 3D patterning outcome of designed muscle organization (left) before and (after) removing the sacrificial material (Pluronic F127). The printed construct was cross-linked with thrombin solution to induce gelation of fibrinogen and the uncross-linked sacrificial material was removed by dissolving with cold medium. (**d**,**e**) The PCL pillar structure is essential to stabilize the 3D printed muscle organization and to induce a compaction phenomenon of the patterns of the cell-laden hydrogel that causes cell alignment in a longitudinal direction of the printed constructs; without PCL pillar (**d**) and with PCL pillar (**e**). The cells with PCL pillar showed unidirectionally organized cellular morphologies that are consistently aligned along the longitudinal axis of the printed construct, which is in contrast to the randomly oriented cellular morphologies without PCL pillar. (**f**) The live/dead staining of the encapsulated cells in the fiber structure indicates high cell viability after the printing process (green: live cells; red: dead cells). (**g**) Immunofluorescent staining for myosin heavy chain of the 3D printed muscle organization after 7-d differentiation. The encapsulated myoblasts aligned along the longitudinal direction of the fiber structure. (**h**–**m**) Structural maintenance and host nerve integration of the bioprinted muscle construct in *in vivo* study. (**h**) Schematic diagram of ectopic implantation of bioprinted muscle construct *in vivo*. (**i**–**k**) The bioprinted muscle construct was subcutaneously implanted with the dissected CPN inserted into the printed muscle construct, and the harvested implants after 2 weeks of implantation showed the presence of organized muscle fibers and innervating capability (α-BTX-positive structures) within the implanted construct, as confirmed by immunostaining using skeletal muscle markers (desmin (**j**) and MHC$^+$ and α-BTX$^+$ structure (arrows) (**k**)). (**l**) The evidence of nerve integration was demonstrated with double staining of neurofilament (NF$^+$) and α-BTX$^+$ structure (arrows). (**m**) The vascularization of implanted muscle construct was confirmed by vWF immunostaining. (**n**) Functional assessment of bioprinted muscle constructs after 4 weeks of implantation (*$P < 0.05$). Positive control: the normal gastrocnemius muscle; negative control: the gluteus muscle after dissected CPN.

© 2016 Nature America, Inc. All rights reserved.

0 mV for the negative controls (subcutaneous tissue), indicating that the implanted muscle constructs responded to electrical stimulation to an extent consistent with immature, developing muscle (**Fig. 6n**).

DISCUSSION

Bioprinters based on jetting, extrusion and LIFT methods can deliver viable cells, biomaterials and macromolecules to generate 3D tissue structures. However, in general they are limited in their ability to generate large biological constructs with sufficient structural integrity for surgical implantation[28–30], and the few *in vivo* studies of bioprinted tissue structures tested less complex constructs with low mechanical stability[35,36]. The ITOP can address the limitations of size and stability by sequentially printing cell-laden hydrogels with a synthetic polymer and a temporary scaffolding, creating tissue constructs with the structural integrity needed for surgical implantation. A computer-generated 3D tissue model can be converted to a motion program that operates and guides the dispensing nozzles to take defined paths for delivery of cells and materials. The cell-laden hydrogel protects cell viability and promotes growth and expansion, whereas the adjacent sacrificial scaffolding provides the initial structural and architectural integrity. As the cells anchored three dimensionally within the hydrogel initiate the transition to tissue formation, they start to secrete their own matrix, replacing the hydrogel as it slowly degrades over time. The system's modular design enables printing of a wide array of tissue constructs. Here we used up to four material repositories, but many additional repositories could be installed to print constructs containing multiple cell types and biomaterials.

Cell carriers for bioprinting must provide adequate mechanical support, cell-specific cues and negligible cytotoxicity. As few such materials are available[37,38], we fulfilled these requirements with a mixture of gelatin, fibrinogen, HA and glycerol. Gelatin was used because of its thermo-sensitive properties: it is liquid above 37 °C, solid below 25 °C. Fibrinogen provides stability to the gel and a microenvironment conducive to cell adhesion and proliferation. HA

and glycerol enhance dispensing uniformity and prevent nozzle clogging. The concentrations of gelatin, fibrinogen, HA and glycerol were optimized to protect cells from physical stress during printing. Although the optimized cell carrier is dispensed as a weak hydrogel, it has the favorable dispensing characteristics of high-viscosity materials, maintaining its position and shape without cross-linking even on porous surfaces. This allowed for the creation of microchannels made of both cell-laden hydrogel and PCL patterns for nutrient and oxygen diffusion into the printed constructs. Most other bioprinters use liquid cell carriers that do not retain their shape. The composition of our composite hydrogel can be adjusted depending on the cell concentration and construct size.

To endow printed constructs with structural strength, we used PCL internally and Pluronic F127 as an external sacrificial scaffold. PCL is biocompatible, flexible, and has a low melting temperature of 60 °C[39], enabling co-printing with cell-laden hydrogel. These properties, together with its rapid cooling after extrusion, and the microchannel distance gap between the PCL and cell-laden hydrogel, minimize cell damage from heat transfer. PCL also has a relatively long degradation time (~1.5 to 2 years)[40], which provides long-term structural stability. In contrast, materials with more rapid degradation often generate byproducts and can cause dimensional deformation[41,42]. Pluronic F127 is easy to print uniformly and structurally strong[24] but is little used in tissue engineering because of its poor cell compatibility[43]. However, printing an outer mold of bio-inert Pluronic F127 simultaneously with the inner tissue construct allows the latter to retain its shape throughout the printing process. Once printing is complete, the Pluronic F127 shell is immediately washed out.

Conventional tissue engineering has demonstrated success in generating bone, cartilage and muscle[44–46], but achieving reproducible, complex architectures that are well vascularized and suitable for clinical use has proved challenging[1,2]. These three tissues have also been fabricated with bioprinters, although only as 2D or small structures[47,48]. The ITOP produces human-scale tissue constructs with complex architectures and high structural integrity. This study demonstrates the feasibility of printing sizable living tissue constructs that mature into vascularized functional tissues *in vivo,* indicating potential utility in translational applications. The application to bone showed that it provides a favorable microenvironment for osteogenic differentiation of hAFSCs *in vitro* and subsequent tissue maturation *in vivo*, consistent with our previous study of bone constructs generated from hAFSCs[32]. The application to cartilage demonstrated generation of a complex, human ear–shaped tissue construct containing cartilage tissue that possesses histological and mechanical characteristics of human auricles after implantation *in vivo*. Finally, the application to skeletal muscle reproduced the structure of native muscle—highly oriented myofiber bundles formed from numerous fused mononucleated muscle cells[49,50]. All three tissue constructs showed promising structural and functional characteristics *in vitro* and *in vivo*.

It is well established that the maximum nutrient diffusion distance for cells to survive without vascularity is ~100–200 μm[51]. Creation of cell constructs larger than this scale requires vascularity. Several approaches have been used to promote mass transfer of nutrients and oxygen in engineered tissues, including growth factors that stimulate angiogenesis[22,52,53]. The ITOP allows for the use of microchannels with a porous lattice design that facilitate nutrient and oxygen diffusion[54–56], extending the diffusion limit. We demonstrated that constructs with microchannels resulted in enhanced tissue formation (**Fig. 5f**). Cartilage structures of 3.2 cm × 1.6 cm × 0.9 cm showed adequate tissue formation without necrosis after 5 weeks *in vitro* (**Fig. 5g**). The bioprinted bone, ear and muscle constructs implanted *in vivo* showed evidence of vascularization without necrosis (**Figs. 4l**, **5i** and **6m**), and the muscle constructs showed the presence of neuromuscular junctions (**Fig. 6k**,**l**).

We used two primary cell types (chondrocytes and hAFSCs) and two cell lines, fibroblasts (3T3) and myoblasts (C2C12), to validate the ITOP. As with all tissue engineering approaches, building human tissues for clinical use requires large numbers of human cells. Obtaining sufficient numbers of primary cells from a small tissue biopsy is feasible and has been performed for numerous tissue engineering applications in humans[57–59]. In this study, we used cell concentration per volume as a standard means of calculating the numbers of cells used to ensure uniform, consistent placement of cells regardless of differences in construct dimensions. Our implantation studies in nude mice and rats—in ectopic sites for cartilage and muscle and an orthotopic site for bone—did not assess therapeutic efficacy but were designed to evaluate cell survival and tissue formation. Implantation of bioprinted bone in a calvarial bone defect model in immune-competent animals showed the formation of mature, vascularized bone tissue in implants retrieved up to 5 months later. However, we did not evaluate the host immune response. In-depth, longer-term studies are needed to improve understanding of regeneration enabled by bioprinted tissues.

In conclusion, the ITOP can generate 3D free-form shapes with multiple types of cells and biomaterials, resulting in various architectures with the potential to form various vascularized tissue types. With further development, this technology may produce clinically useful tissues and organs that incorporate multiple cell types at precise locations to recapitulate native structure and function.

METHODS

Methods and any associated references are available in the online version of the paper.

Note: Any Supplementary Information and Source Data files are available in the online version of the paper.

ACKNOWLEDGMENTS

This work was supported, in part, by grants from the Armed Forces Institute of Regenerative Medicine (W81XWH-08-2-0032), the Telemedicine and Advanced Technology Research Center at the US Army Medical Research and Material Command (W81XWH-07-1-0718) and the Defense Threat Reduction Agency (N66001-13-C-2027). We would like to thank D.M. Eckman for editorial comments on this manuscript, and H.S. Kim and G.V. Kulkarni for technical assistance.

AUTHOR CONTRIBUTIONS

H.-W.K., S.J.L., J.J.Y. and A.A. developed the concept of the integration tissue and organ printing (ITOP) system and designed all experiments. H.-W.K. performed *in vitro* experiments and composite hydrogel development, analyzed data and wrote the manuscript. C.K. performed *in vivo* experiments of the printed cartilage and bone constructs and analyzed data. I.K.K. performed *in vivo* experiments of the printed skeletal muscle construct and analyzed data. S.J.L., J.J.Y. and A.A. analyzed data and wrote the manuscript. A.A. provided direction and supervised the project. S.J.L., J.J.Y. and A.A. edited the manuscript.

COMPETING FINANCIAL INTERESTS

The authors declare no competing financial interests.

Reprints and permissions information is available online at http://www.nature.com/reprints/index.html.

1. Mikos, A.G. *et al.* Engineering complex tissues. *Tissue Eng.* **12**, 3307–3339 (2006).
2. Atala, A., Kasper, F.K. & Mikos, A.G. Engineering complex tissues. *Sci. Transl. Med.* **4**, 160rv12 (2012).
3. Murphy, S.V. & Atala, A. 3D bioprinting of tissues and organs. *Nat. Biotechnol.* **32**, 773–785 (2014).
4. Mironov, V. *et al.* Organ printing: tissue spheroids as building blocks. *Biomaterials* **30**, 2164–2174 (2009).

© 2016 Nature America, Inc. All rights reserved.

5. Jones, N. Science in three dimensions: the print revolution. *Nature* **487**, 22–23 (2012).
6. Ferris, C.J., Gilmore, K.G., Wallace, G.G. & In het Panhuis, M. Biofabrication: an overview of the approaches used for printing of living cells. *Appl. Microbiol. Biotechnol.* **97**, 4243–4258 (2013).
7. Xu, T. *et al.* Complex heterogeneous tissue constructs containing multiple cell types prepared by inkjet printing technology. *Biomaterials* **34**, 130–139 (2013).
8. Durmus, N.G., Tasoglu, S. & Demirci, U. Bioprinting: Functional droplet networks. *Nat. Mater.* **12**, 478–479 (2013).
9. Cooper, G.M. *et al.* Inkjet-based biopatterning of bone morphogenetic protein-2 to spatially control calvarial bone formation. *Tissue Eng. Part A* **16**, 1749–1759 (2010).
10. Costa, K.D., Lee, E.J. & Holmes, J.W. Creating alignment and anisotropy in engineered heart tissue: role of boundary conditions in a model three-dimensional culture system. *Tissue Eng.* **9**, 567–577 (2003).
11. Cui, X., Breitenkamp, K., Finn, M.G., Lotz, M. & D'Lima, D.D. Direct human cartilage repair using three-dimensional bioprinting technology. *Tissue Eng. Part A* **18**, 1304–1312 (2012).
12. da Graca, B. & Filardo, G. Vascular bioprinting. *Am. J. Cardiol.* **107**, 141–142 (2011).
13. Duan, B., Hockaday, L.A., Kang, K.H. & Butcher, J.T. III. Bioprinting of heterogeneous aortic valve conduits with alginate/gelatin hydrogels. *J. Biomed. Mater. Res. A* **101**, 1255–1264 (2013).
14. Ilkhanizadeh, S., Teixeira, A.I. & Hermanson, O. Inkjet printing of macromolecules on hydrogels to steer neural stem cell differentiation. *Biomaterials* **28**, 3936–3943 (2007).
15. Norotte, C., Marga, F.S., Niklason, L.E. & Forgacs, G. Scaffold-free vascular tissue engineering using bioprinting. *Biomaterials* **30**, 5910–5917 (2009).
16. Skardal, A., Zhang, J. & Prestwich, G.D. Bioprinting vessel-like constructs using hyaluronan hydrogels crosslinked with tetrahedral polyethylene glycol tetracrylates. *Biomaterials* **31**, 6173–6181 (2010).
17. Xu, T. *et al.* Hybrid printing of mechanically and biologically improved constructs for cartilage tissue engineering applications. *Biofabrication* **5**, 015001 (2013).
18. Derby, B. Printing and prototyping of tissues and scaffolds. *Science* **338**, 921–926 (2012).
19. Mironov, V., Boland, T., Trusk, T., Forgacs, G. & Markwald, R.R. Organ printing: computer-aided jet-based 3D tissue engineering. *Trends Biotechnol.* **21**, 157–161 (2003).
20. Cui, X. & Boland, T. Human microvasculature fabrication using thermal inkjet printing technology. *Biomaterials* **30**, 6221–6227 (2009).
21. Khalil, S. & Sun, W. Bioprinting endothelial cells with alginate for 3D tissue constructs. *J. Biomech. Eng.* **131**, 111002 (2009).
22. Lee, W. *et al.* Multi-layered culture of human skin fibroblasts and keratinocytes through three-dimensional freeform fabrication. *Biomaterials* **30**, 1587–1595 (2009).
23. Xu, T., Baicu, C., Aho, M., Zile, M. & Boland, T. Fabrication and characterization of bio-engineered cardiac pseudo tissues. *Biofabrication* **1**, 035001 (2009).
24. Chang, C.C., Boland, E.D., Williams, S.K. & Hoying, J.B. Direct-write bioprinting three-dimensional biohybrid systems for future regenerative therapies. *J. Biomed. Mater. Res. B Appl. Biomater.* **98**, 160–170 (2011).
25. Fedorovich, N.E., De Wijn, J.R., Verbout, A.J., Alblas, J. & Dhert, W.J. Three-dimensional fiber deposition of cell-laden, viable, patterned constructs for bone tissue printing. *Tissue Eng. Part A* **14**, 127–133 (2008).
26. Jakab, K., Neagu, A., Mironov, V., Markwald, R.R. & Forgacs, G. Engineering biological structures of prescribed shape using self-assembling multicellular systems. *Proc. Natl. Acad. Sci. USA* **101**, 2864–2869 (2004).
27. Landers, R., Hübner, U., Schmelzeisen, R. & Mülhaupt, R. Rapid prototyping of scaffolds derived from thermoreversible hydrogels and tailored for applications in tissue engineering. *Biomaterials* **23**, 4437–4447 (2002).
28. Hoffman, A.S. Hydrogels for biomedical applications. *Adv. Drug Deliv. Rev.* **54**, 3–12 (2002).
29. Nicodemus, G.D. & Bryant, S.J. Cell encapsulation in biodegradable hydrogels for tissue engineering applications. *Tissue Eng. Part B Rev.* **14**, 149–165 (2008).
30. Wang, X., Yan, Y. & Zhang, R. Recent trends and challenges in complex organ manufacturing. *Tissue Eng. Part B Rev.* **16**, 189–197 (2010).
31. Guillotin, B. & Guillemot, F. Cell patterning technologies for organotypic tissue fabrication. *Trends Biotechnol.* **29**, 183–190 (2011).
32. De Coppi, P. *et al.* Isolation of amniotic stem cell lines with potential for therapy. *Nat. Biotechnol.* **25**, 100–106 (2007).
33. Kim, J. *et al.* In vitro osteogenic differentiation of human amniotic fluid-derived stem cells on a poly(lactide-co-glycolide) (PLGA)-bladder submucosa matrix (BSM) composite scaffold for bone tissue engineering. *Biomed. Mater.* **8**, 014107 (2013).
34. Bian, W., Juhas, M., Pfeiler, T.W. & Bursac, N. Local tissue geometry determines contractile force generation of engineered muscle networks. *Tissue Eng. Part A* **18**, 957–967 (2012).
35. Binder, K.W. *et al.* In situ bioprinting of the skin for burns. *J. Am. Coll. Surg.* **211**, 7 (2010).
36. Marga, F. *et al.* Toward engineering functional organ modules by additive manufacturing. *Biofabrication* **4**, 022001 (2012).
37. Schuurman, W. *et al.* Bioprinting of hybrid tissue constructs with tailorable mechanical properties. *Biofabrication* **3**, 021001 (2011).
38. Shim, J.-H., Lee, J.-S., Kim, J.Y. & Cho, D.-W. Bioprinting of a mechanically enhanced three-dimensional dual cell-laden construct for osteochondral tissue engineering using a multi-head tissue/organ building system. *J. Micromech. Microeng.* **22**, 085014 (2012).
39. Serrano, M.C. *et al.* In vitro biocompatibility assessment of poly(epsilon-caprolactone) films using L929 mouse fibroblasts. *Biomaterials* **25**, 5603–5611 (2004).
40. Sun, H., Mei, L., Song, C., Cui, X. & Wang, P. The in vivo degradation, absorption and excretion of PCL-based implant. *Biomaterials* **27**, 1735–1740 (2006).
41. Ignatius, A.A. & Claes, L.E. In vitro biocompatibility of bioresorbable polymers: poly(L, DL-lactide) and poly(L-lactide-co-glycolide). *Biomaterials* **17**, 831–839 (1996).
42. Zignani, M. *et al.* Improved biocompatibility of a viscous bioerodible poly(ortho ester) by controlling the environmental pH during degradation. *Biomaterials* **21**, 1773–1778 (2000).
43. Lippens, E. *et al.* Cell survival and proliferation after encapsulation in a chemically modified Pluronic(R) F127 hydrogel. *J. Biomater. Appl.* **27**, 828–839 (2013).
44. Amini, A.R., Laurencin, C.T. & Nukavarapu, S.P. Bone tissue engineering: recent advances and challenges. *Crit. Rev. Biomed. Eng.* **40**, 363–408 (2012).
45. Bichara, D.A. *et al.* The tissue-engineered auricle: past, present, and future. *Tissue Eng. Part B Rev.* **18**, 51–61 (2012).
46. Ostrovidov, S. *et al.* Skeletal muscle tissue engineering: methods to form skeletal myotubes and their applications. *Tissue Eng. Part B Rev.* **20**, 403–436 (2014).
47. Ker, E.D. *et al.* Bioprinting of growth factors onto aligned sub-micron fibrous scaffolds for simultaneous control of cell differentiation and alignment. *Biomaterials* **32**, 8097–8107 (2011).
48. Phillippi, J.A. *et al.* Microenvironments engineered by inkjet bioprinting spatially direct adult stem cells toward muscle- and bone-like subpopulations. *Stem Cells* **26**, 127–134 (2008).
49. Choi, J.S., Lee, S.J., Christ, G.J., Atala, A. & Yoo, J.J. The influence of electrospun aligned poly(epsilon-caprolactone)/collagen nanofiber meshes on the formation of self-aligned skeletal muscle myotubes. *Biomaterials* **29**, 2899–2906 (2008).
50. Wakelam, M.J. The fusion of myoblasts. *Biochem. J.* **228**, 1–12 (1985).
51. Jain, R.K., Au, P., Tam, J., Duda, D.G. & Fukumura, D. Engineering vascularized tissue. *Nat. Biotechnol.* **23**, 821–823 (2005).
52. Boland, T., Xu, T., Damon, B. & Cui, X. Application of inkjet printing to tissue engineering. *Biotechnol. J.* **1**, 910–917 (2006).
53. Lee, Y.-B. *et al.* Bio-printing of collagen and VEGF-releasing fibrin gel scaffolds for neural stem cell culture. *Exp. Neurol.* **223**, 645–652 (2010).
54. Cabodi, M. *et al.* A microfluidic biomaterial. *J. Am. Chem. Soc.* **127**, 13788–13789 (2005).
55. Ling, Y. *et al.* A cell-laden microfluidic hydrogel. *Lab Chip* **7**, 756–762 (2007).
56. Stachowiak, A.N., Bershteyn, A., Tzatzalos, E. & Irvine, D.J. Bioactive hydrogels with an ordered cellular structure combine interconnected macroporosity and robust mechanical properties. *Adv. Mater.* **17**, 399–403 (2005).
57. Atala, A., Bauer, S.B., Soker, S., Yoo, J.J. & Retik, A.B. Tissue-engineered autologous bladders for patients needing cystoplasty. *Lancet* **367**, 1241–1246 (2006).
58. Raya-Rivera, A. *et al.* Tissue-engineered autologous urethras for patients who need reconstruction: an observational study. *Lancet* **377**, 1175–1182 (2011).
59. Raya-Rivera, A.M. *et al.* Tissue-engineered autologous vaginal organs in patients: a pilot cohort study. *Lancet* **384**, 329–336 (2014).

© 2016 Nature America, Inc. All rights reserved.

ONLINE METHODS

Integrated tissue and organ printer. The integrated tissue and organ printing (ITOP) is composed of an XYZ stage/controller, dispensing module, and a closed chamber (**Fig. 1a** and **Supplementary Fig. 1**). A three-axis stage system (Aerotech, Inc., Pittsburgh, PA) having 200 × 200 × 100 mm^3 travel and controller (Aerotech, Inc.) were used to provide printing paths for the 3D bioprinting process. The resolutions of this system were 250 nm and 500 nm for the XY axes and the Z axis, respectively. The dispensing module consisted of a precision pneumatic pressure controller (ML-808FXcom; Musashi Engineering, Inc., Tokyo, Japan), syringe heater (TB-10E-K; Musashi Engineering, Inc.), syringe (Musashi Engineering, Inc.) and nozzle (Musashi Engineering, Inc.). Finally, the closed-chamber system was constructed by equipping a temperature controller (ThermoTEC; EIC Solutions, Inc., Warminster, PA) and a humidifier (AOS 7146, AIR-O-SWISS, Widnau, Switzerland) in the customized acrylic enclosure.

The ITOP is made up of multiple cartridges to individually deliver various synthetic polymers and/or cell-laden hydrogels of various cell types. We have employed the extrusion-method used in Fused Deposition Modeling (FDM) to design this novel ITOP concurrently with computer aided-design and computer aided-manufacturing (CAD/CAM) to produce living tissue constructs with complex shape and large size.

Generation of motion program. The process can be started by scanning the patient to obtain 3D volumetric information on a target tissue or organ using medical imaging modalities such as CT and MRI. The imaging tools acquire information from cross-sectional slices of the body, and the data are stored in the Digital Imaging and Communications in Medicine (DICOM) format. This format is then transformed into a 3D CAD model by a medical image processing software, Mimics (Materialise, Leuven, Belgium). The CAD model is converted to a motion program, which describes the operation of the dispensing nozzles using a customized software developed with Visual Studio 6.0 (Microsoft, Redmond, WA) which generated the motion programs transferred from the CAD model. This software was constructed by slicing and path-generation algorithms, which are used in rapid prototyping technology[60,61]. The slicing process is used to obtain information of the sliced profile of a CAD model at a specific height. The information is generated by geometric calculation of intersected lines between a plane of specific height and triangular facets composing a stereolithography (STL) model, which is a standardized file format to store 3D CAD model, and it is generally used in 3D printing. Path generation is conducted by applying a user-defined strategy to the sliced profile. For this purpose, we used a parallel line hatching method[61]. Intersection points between the profile and user-defined parallel lines were calculated, and the tool path information was generated by gathering parallel lines that are positioned inside of the profile. The generated path information is combined with other fabrication information such as scanning speed, air pressure and dispensing material, and transformed to text-based motion program. Finally, this motion program is transferred to the operating computer for printing the 3D tissue architectures.

Preparation of cell carrier material, synthetic polymer and sacrificial hydrogel. Three components were used to produce the 3D architectures: composite hydrogel, PCL polymer and Pluronic F-127. The composite hydrogel as a cell carrier material is a mixture of gelatin (G6411), fibrinogen (F8630), HA (53747) and glycerol (G2025), which were purchased from Sigma-Aldrich (St. Louis, MO). Briefly, HA was dissolved in DMEM by stirring the solution at 37 °C overnight. Glycerol was added into the solution and stirred for 1 h. The solution was gently shaken after adding the gelatin and fibrinogen for 1 h. The procedure resulted in final concentrations of gelatin (35~45 mg/ml), fibrinogen (20–30 mg/ml), HA (3 mg/ml) and glycerol (10% v/v). The final concentrations of this composite hydrogel were optimized for each target tissue (**Table 1**). The prepared solution was sterilized by filtration through a 0.45-μm syringe filter and was stored at −20 °C before use. The cells were gently mixed with this composite solution in a water bath at 37 °C. As a supporting material, PCL (Mw; 43,000~50,000, Polysciences, Inc., Warrington, PA) was used through the melting process. For sacrificial material, Pluronic F-127 in powder form (P2443; Sigma-Aldrich) was added to a 10% v/v glycerol solution at a final concentration of 33% w/v. The solution was slowly shaken at 4 °C for 1~2 d and stored at 4 °C.

2D and 3D printing process. This cell-laden composite hydrogel and Pluronic F-127 were loaded into plastic syringes. PCL polymer was loaded into a metal syringe which was heated at 92.5 °C for melting. In the printing process, the cell-laden hydrogel was printed through a 300-μm Teflon nozzle at 50~80 KPa of air pressure and the Pluronic F127 was printed through a 250-μm metal nozzle at 200~300 KPa of air pressure. The PCL polymer was printed through a 250-μm cone-shaped metal nozzle at 800 KPa of air pressure. The temperature in the chamber was maintained at 18 °C during the printing process. After printing, the printed 3D architectures were cross-linked by the addition of a thrombin solution (20 UI/ml, T4648, Sigma-Aldrich) for 30 min at room temperature. Then, the Pluronic F127 was washed out with cold PBS solution for three times (3 min/wash), and the PBS solution was exchanged with culture medium.

Cell culture. Four cell types were used; 3T3 fibroblasts (ATCC, Manassas, VA), C2C12 myoblasts (ATCC), human amniotic fluid-derived stem cells (hAFSCs) and rabbit primary auricular chondrocytes. 3T3 fibroblasts were used for hydrogel optimization and initial 3D patterning. Briefly, cells were cultured in high glucose Dulbecco's Modifies Eagle Medium (DMEM, Life Technologies, Carlsbad, CA) supplemented with 10% FBS (FBS), 1% penicillin/streptomycin. Red and green cell labeling was performed using the Vybrant Multicolor Cell Labeling kit (V-22889; Life Technologies) according to the manufacturer's instruction.

Human AFSCs were used for printing the mandible bone structures. The isolation of hAFSCs has been previously described[32]. Briefly, human amniocentesis cultures were harvested by trypsinization, and subjected to c-kit immunoselection. Human AFSCs (H1 cell line) were received at passage 17 and cultured in α-Minimum Essential Medium (α-MEM) supplemented with 15% ES-FBS, 18% Chang B (Irvine Scientific, Santa Ana, CA), 2% Chang C (Irvine Scientific), 100 U/ml penicillin, 100 μg/ml streptomycin, and 2 mM L-glutamine. For osteogenic differentiation, the 3D architecture of the mandible bone structure was cultured in low glucose DMEM medium, 10% FBS and 1% penicillin/streptomycin with osteogenic supplements (100 nM dexamethasone (Sigma), 10 mM β-glycerol phosphate (Sigma), 50 μM ascorbic acid 2-phosphate (Sigma)).

Auricular chondrocytes used for printing human ear structures were isolated from New Zealand White rabbits (male, 2.5–3.5 kg, Charles River Labs., Inc., Wilmington, MA) by digesting with collagenase type I[62]. The isolated chondrocytes were cultured in DMEM/F-12 mixture with 10% FBS, 1% penicillin/streptomycin and 0.25 μg/ml amphotericin B. The printed 3D ear constructs were cultured in DMEM/F-12 with 10 ng/ml transforming growth factor β3 (TGF-β3) (ProSpec-Tany TechnoGene Ltd., Rehovot, Israel), 50 μg/ml L-ascorbic acid 2-phosphate (Sigma), 100 nM dexamethasone (Sigma), 50 mg/ml ITS premix (BD, Franklin Lakes, NJ), 1% penicillin/streptomycin and 0.25 μg/ml amphotericin B. 20 μg/ml aprotinin (Sigma) was added to the culture medium to inhibit enzyme activity and stabilize the 3D architecture.

C2C12 myoblasts used for printing skeletal muscle constructs were cultured in high glucose DMEM supplemented with 10% FBS and 1% penicillin/streptomycin. For muscle cell differentiation, the printed 3D muscle constructs were cultured in DMEM/F-12 mixture containing 1% horse serum and 1% penicillin/streptomycin. All reagents for cell culture were purchased from Gibco Cell Culture (Life Technologies).

3T3 fibroblasts and C2C12 myoblasts were verified with phase contrast microscopy using cellular morphology, growth characteristics and comparison with reference images. Specifically, C2C12 myoblasts were validated via myotube formation. Both cell lines were tested and were mycoplasma-free.

Cell viability. Live/dead viability/cytotoxicity kit (L-3224; Life Technologies) was used for determining cell viability within the printed 3D constructs according to the manufacturer's instructions. Briefly, an assay solution containing 0.5 μl/ml Cal-AM and 2 μl/ml Eth-D was prepared in PBS. After washing the 3D printed patterns with PBS, the assay solution was added to the samples

© 2016 Nature America, Inc. All rights reserved.

incubated at room temperature for 2 h. Fluorescence microscopy was used to evaluate the live/dead staining of cells in the printed constructs. Total six fluorescence images from each sample were taken: three images from the top of sample and another three images were taken from bottom. In the images, the live cells are shown as green and dead cells are red. The number of live and dead cell was manually counted. After counting live and dead cells, cell viability was calculated by dividing the number of live cells (confirmed by Trypan Blue staining before the printing process) by the total number of cells in the printed constructs.

Cell proliferation. AlamarBlue assay kit (DAL1100; Life Technologies) was used to measure cell proliferation within the printed constructs according to the manufacturer's instruction. Briefly, after mixing the assay solution with cell culture medium at a 1:10 volume ratio, 500 µl/ml of this mixture was added to each construct and incubated for 2 h at 37 °C. After incubation, 100 µl of assay solution from each sample was placed into the wells of a 96-well plate and fluorescence intensity was measured using a microplate reader at the excitation/emission of 544 nm/590 nm (SpectraMax M5, Molecular Devices, Sunnyvale, CA). After removing all assay solution and washing the samples twice with PBS, the samples were cultured further for use in the next experiment.

Mandible bone reconstruction. The mineralized extracellular matrix secreted by hAFSCs was evaluated using Alizarin Red S staining. Calcium deposition that had occurred in the printed mandible bone structure containing hAFSCs was visualized using Alizarin Red S staining at 28 d of osteogenic differentiation. Briefly, the printed bone tissue constructs were washed three times with PBS and fixed in ice-cold 70% ethanol for 1 h. Following a rinse with deionized water, the constructs were stained in 40 mM Alizarin Red S solution (pH 4.2) for 10 min. After several washes with deionized water, images of stained samples were taken using a digital microscope (AD413TL, AnMo Electronics, Taipei).

Calvarial bone reconstruction. The bioprinted constructs for calvarial bone reconstruction were composed of PCL doped with tricalcium phosphate (TCP) nanoparticles (Berkeley Advanced Biomaterials, Berkeley, CA) at a 1:1 ratio by weight and cell-laden hydrogel dispensed in an interleaved crosshatch pattern. The mixture of PCL and TCP was printed through a 200-µm diameter nozzle (TECDIA Inc., Campbell, CA) with 780 kPa compressed air. These materials were heated to 112 °C in the heating chamber of ITOP to produce a beam width of 200 µm. The printed PCL/TCP architecture provided an internal porosity of approximately 70%. The top and bottom surfaces of the construct were printed with beam heights of 50 µm and 220 µm pitch resulting in 100-µm thick region of low porosity to minimize host cell infiltration.

The cell-laden hydrogel was printed within the internal pores of the PCL/TCP structure, which was produced with 115 µm beam height and 670 µm pitch with repeating layers such that resultant wall heights reached 345 µm. The cell-laden hydrogel was composed of 5×10^6 hAFSCs per ml of the hydrogel described above and printed through a 300 µm diameter Teflon-lined needle nozzle (Musashi Engineering Inc.) at 60 kPa. After printing, constructs were treated with a thrombin solution to induce fibrinogen conversion to fibrin, as well as osteogenic culture conditions. Constructs were incubated in osteogenic differentiation media for 10 d before implantation.

Rats (Sprague Dawley) weighing 250–300 g were purchased from Charles River. The top of the cranium was exposed by a midline incision through skin and periosteum after anesthetization with isoflurane. A trephine burr was used to drill an 8-mm diameter defect in the center of the calvarial bone. After the implant was inserted into the defect, the incision was closed in layers using 3-0 and 4-0 sutures. The cutaneous sutures were removed 10–14 d after surgery. Animals were euthanized by CO_2 asphyxiation. Samples were fixed for 48 h in 10% buffered formalin, with one change after 24 h, then decalcified in Richard Allen Scientific Decalcifying Solution (Thermo Scientific). Samples were embedded in paraffin for sectioning and staining. Sections were stained with H&E and modified tetrachrome. Immunostaining for the vascularization was performed using a primary antibody, von Willebrand factor (vWF; 1:400, cat. no. A0082, DAKO, Carpinteria, CA) and developed with ImmPRESS DAB chromagen (Vector Labs, Burlingame, CA).

Ear cartilage reconstruction. The printed ear tissue constructs were prepared for histological analysis by fixation in 10% phosphate-buffered formalin at room temperature for 24 h. Subsequently, the samples were embedded in paraffin and sectioned into 5 µm sections. Deparaffinized sections were stained with Safranin-O, which confirmed the cellular morphology and glycosaminoglycans (GAG) production. Briefly, the samples were incubated with 0.1% Safranin-O dye solution followed by Weigert's iron hematoxylin. Fast green solution (0.01%) was used as a counter stain for identification of nuclei and cytoplasm. The stained images were taken using a light microscope (DM4000 B, Leica Microsystems, Wetzlar, Germany).

For the *in vivo* animal studies, the printed ear constructs were implanted in dorsal subcutaneous pockets in athymic nude mice). After implantation, the skin was closed with Vicryl 6-0 sutures. All animal studies were conducted in accordance with Wake Forest University Animal Care and Use Committee (ACUC) regulations. The implanted ear constructs were harvested after 1 and 2 months and the constructs were evaluated by H&E and Safranin-O staining as described above. For immunostaining, the formalin-fixed ear constructs were subjected to pepsin antigen retrieval at 37 °C for 20 min and blocked in serum-free blocking solution (Vector Labs), and incubated with primary antibody for collagen type II (1:30; Southern Biotech, cat. no. 1320-01, Birmingham, AL) and vWF (1:400, DAKO).

The Blyscan Sulfated Glycosaminoglycan Assay kit (Biocolor Ltd., Antrim, UK) was used to measure GAG contents (µg/mg of wet weight of tissue) in the native ear cartilage and the implanted printed ear constructs by colorimetric quantification according to the manufacturer's instruction. Measurements from standards set the concentration curve that was used to determine test sample concentrations.

In order to evaluate the mechanical properties of the implanted ear constructs, three-point bending was conducted to assess the mechanical strength of the printed constructs after printing and after *in vivo* implantation. Rabbit ear cartilage was also cut to the same dimensions and tested as positive controls. Bending support struts were placed 5 mm apart and an extension of 2 mm was conducted at a rate of 1.2 mm/min[63]. Each specimen was subjected to serial bending in order to see plastic deformation after four cycles. Resilience of the tissue was interrogated by 3-point bending and the results were quantified as follows.

$$\Delta Load\%^{C0-n} = 100 \times \left(\frac{F^{Cn} - F^{C0}}{F^{C0}} \right)$$

where C_0 is initial cycle and C_n is the nth cycle. The bending assay shows if fatigue occurs gradually throughout testing ($C_{1\text{-}4}$), as seen in native tissue, or more specifically fails in the beginning ($C_{1\text{-}2}$) or end of testing ($C_{2\text{-}4}$). Calculations were performed to ascertain the average difference in normalized loading at 50% extension between cycles 1-2 and 1-4.

Skeletal muscle organization. Immunohistochemical staining for myosin heavy chain (MHC) was performed to evaluate myotube formation within the 3D printed constructs. Briefly, the samples were incubated with MF-20 antibody (1 µg/ml) (Developmental Studies Hybridoma Bank, Iowa City, IA) for 1 h. The samples were then incubated in the secondary AlexaFluor 488 goat anti-mouse IgG (Life Technologies) for 30 min. Finally, the samples were visualized and photographed with a Zeiss microscope (M1, Zeiss Axio Imager, Carl Zeiss, Jena, Germany) using Axiovision Software (Carl Zeiss).

In vivo animal studies were performed with a subcutaneous (ectopic) implantation method[64]. Nude rats (male, 14–16 weeks, Charles River Labs.) were used for this study. In brief, under anesthesia (isoflurane), the animals received a long incision on the skin of the hind limb, dissection of the skin and the gluteus muscle, exposure of the sciatic nerve, resection of the distal end of the CPN, and placing the dissected CPN on the fascia of the gluteus muscle beneath the skin. The proximal stump of CPN was embedded within the bioprinted muscle constructs ($15 \times 5 \times 1$ mm^3; **Fig. 5h**,**i**). The bioprinted muscle constructs were implanted in the subcutaneous space over the gluteal muscle, separated by fascia and subcutaneous tissue. Therefore, there was no direct contact between the implant and native gluteal muscle. There was no gross adhesion or contact with the native gluteal muscle at retrieval.

© 2016 Nature America, Inc. All rights reserved.

doi:10.1038/nbt.3413

At 2 weeks after implantation, the tissue construct was harvested for immunohistological analysis.

For immunostaining, the formalin-fixed tissue constructs were permeabilized with methanol at below 20 °C, blocked with serum-free blocking solution and incubated with primary antibody for desmin (1:50, Santa Cruz Biotechnology, Inc., cat. no. sc-23879), MHC (MF20, 1:500, Developmental Studies Hybridoma Bank), neurofilament (NF) (1:100, Abcam, cat. no. Ab24571, Cambridge, MA) and vWF (1:400, DAKO). For double staining with alpha-bungarotoxin (α-BTX, Life Technologies) for innervation characterization, the section was initially incubated with AlexaFluor 488 labeled α-BTX. As secondary antibody, AlexaFluor 488- or 594-labeled goat anti-mouse antibody (Life Technologies) was used. All images were acquired with a fluorescent microscope (Leica DM 8000).

For functional evaluation, electromyography (EMG) was performed to measure the activities of the leg muscles affected by the nerve injury. Under anesthesia, the sciatic nerve area was exposed. A disposable monopolar needle electrode (25 mm × 0.45 mm, 26G; Cadwell Labs., Inc., Kennewick, WA) was used. The ground electrode was put on the back of the animal, and stimuli were applied using a hook-shaped bipolar tungsten electrode. A recording electrode was placed in the implant site, and a reference electrode was placed at the distal area of the implant. The sciatic nerve was electrically stimulated with 10.0 mA using a generator. Electrodiagnostics were performed using the Cadwell-Sierra LT EMG setup (Cadwell Labs., Inc.). Digitalized data were stored on a personal computer, and amplitude of the compound muscle action potential (CMAP) of the implanted muscle construct was calculated from these data. As control, CMAP of the gastrocnemius muscle and nonimplanted site was obtained.

Statistical analysis. All results are expressed as mean ± s.d. Differences between experimental groups were analyzed using one-way ANOVA and Tukey post-test. Levene's F-test was used for coefficient of variation (COV) values. A value of $P < 0.05$ was considered as statistically significant.

60. Liao, Y.S. & Chiu, Y.Y. A new slicing procedure for rapid prototyping systems. *Int. J. Adv. Manuf. Technol.* **18**, 579–585 (2001).
61. Park, S.C. & Choi, B.K. Tool-path planning for direction-parallel area milling. *Comput. Aided Des.* **32**, 17–25 (2000).
62. Lee, S.J., Broda, C., Atala, A. & Yoo, J.J. Engineered cartilage covered ear implants for auricular cartilage reconstruction. *Biomacromolecules* **12**, 306–313 (2011).
63. Roy, R. *et al.* Analysis of bending behavior of native and engineered auricular and costal cartilage. *J. Biomed. Mater. Res. A* **68**, 597–602 (2004).
64. Ko, I.K. *et al.* The effect of in vitro formation of acetylcholine receptor (AChR) clusters in engineered muscle fibers on subsequent innervation of constructs in vivo. *Biomaterials* **34**, 3246–3255 (2013).

© 2016 Nature America, Inc. All rights reserved.